

## VVER steel corrosion during in-vessel retention of corium melt

S.V. Bechta<sup>1</sup>, V.S. Granovsky<sup>1</sup>, V.B. Khabensky<sup>1</sup>, E.V. Krushinov<sup>1</sup>, S.A. Vitol<sup>1</sup>, V.F. Strizhov<sup>2</sup>, D. Bottomley<sup>3</sup>, M. Fischer<sup>4</sup>, P. Piluso<sup>5</sup>, A. Miassoedov<sup>6</sup>, W. Tromm<sup>6</sup>, E. Altstadt<sup>7</sup>, H. G. Willschutz<sup>7</sup>, F. Fichot<sup>8</sup>, O. Kymalainen<sup>9</sup>

- |                                                                         |                                                     |
|-------------------------------------------------------------------------|-----------------------------------------------------|
| 1) Aleksandrov Research Institute of Technology, NITI, Sosnovy Bor (RU) | 6) Forschungszentrum Karlsruhe, FZK, Karlsruhe (DE) |
| 2) Nuclear Safety Institute, IBRAE, Moscow (RU)                         | 7) Forschungszentrum Dresden, FZD, Dresden (DE)     |
| 3) Joint Research Centre, ITU, Karlsruhe (EU)                           | 8) IRSN/DPAM/SEMCA, St Paul lez Durance (FR)        |
| 4) AREVA NP GmbH, Erlangen (DE)                                         | 9) FORTUM Nuclear services Ltd, Espoo (FI)          |
| 5) CEA, DEN, Cadarache, St Paul lez Durance (FR)                        |                                                     |

### Abstract

Physicochemical phenomena taking place at the corium-steel interaction during the external cooling of reactor vessel can result in high-temperature steel corrosion and thinning of the vessel wall. The ISTC METCOR project's experimental studies have shown that the main factors influencing corrosion depth and kinetics are oxygen potential, melt composition and steel interfacial temperature but also melt – vessel heat flux.

Experimental data are used for building a model for VVER vessel steel corrosion under corium thermochemical loads and for correlations to quantitatively analyze the influence of corrosion on the reactor vessel thinning. The finite-element calculations, in which the developed models of corrosion and heat transfer in corium pool were used, were able to reproduce the temperature and stress-and-strain vessel condition.

### A INTRODUCTION

The in-vessel corium retention (IVR) is one of the applied strategies to mitigate the effect of a severe accident. The IVR approach has been chosen for the Loviisa NPP with VVER-440 reactors [1]; it is also incorporated into the developed NPP designs with light water reactors [2-6]. The IVR efficiency mostly depends on sufficient margins against departure from nucleate boiling on the external water-cooled vessel surface. To a lesser extent it depends on the vessel damage caused by the thermomechanical stress. But such damage, in principle, cannot be excluded. For this reason it is discussed in the current paper.

High decay heat and a limited surface of heat transfer from the molten pool to the lower head and then to the cooling water lead to a partial melting of the vessel wall. Another phenomenon resulting in the wall thinning is the steel corrosion caused by the physicochemical interaction with molten corium. The experimental studies [7] have determined that the minimum temperature at which the vessel steel corrosion takes place at the interface boundary with the molten steel/Zr layer is 1300°C. The GEMINI2-based thermodynamical calculations given in [8] determined the boundary temperature for similar

conditions with a metallic melt containing Zr, U and some other admixtures. For the latter case it was 1100°C.

In a general case the steel vessel wall can interact both with metallic and oxidic melts. Depending on the oxygen potential of the melt the interaction can follow quite different mechanisms. At a low oxygen potential (corium oxidation index<sup>1</sup>  $C_n < 100\%$ ), the corium-steel interaction can lead to the eutectic melting (dissolution) of steel surface layer, while at high oxygen potentials it can lead to oxidation. The pool composition and macrostructure depend on the reactor unit design and accident scenario, which, in turn, determine the melt oxygen potential. The experimental data of the OECD MASCA project [9] have shown that there are unmixable metallic and oxidic melt layers and that metal layer can be either on the surface or in the bottom of the pool depending on oxygen potentials of initial corium and mass fractions of steel in the melt. However an atmosphere with high content of steam/air mixture may cause oxidation of the metal and formation of a fully-oxidized single-liquid molten pool.

Systematic experimental studies of the physicochemical interaction between the prototypic corium and VVER steel have been performed within the ISTC METCOR project. Its data output is used in the current work for assessing the influence of corrosion on the vessel integrity in IVR conditions.

## B VESSEL STEEL CORROSION MECHANISMS

METCOR experiments tested the VVER-1000 15Kh2NMFA-A steel (C-0.17; Si-0.24; Mn-0.5; Cr-1.93; Ni-1.28; Mo-0.52; V-0.08 mass.%) in the RASPLAV facility, which uses the technology of induction melting in a cold crucible [10]. The design of induction furnaces for the corium-steel interaction studies had minor modifications [11-14], partially made to provide the above-melt steam atmosphere.

In all experiments the cylindrical vessel-steel specimens with embedded thermocouples were placed on the crucible bottom. The molten pool of 1.5...2.0 kg mass was produced on the top surface of vessel steel specimen. Water cooling was provided for the specimens, but a part of the corium - specimen heat flux was evacuated from the specimen side to the water-cooled crucible sections through the side thermal insulation. During the experiment the corrosion depth was continuously measured by the ultrasonic sounding. The melt surface temperature and electric parameters of the induction furnace were measured as well. The experimental methodologies and procedures are described in more detail in references [11-14].

In each experiment the steel corrosion was investigated under steady state conditions during a period of time sufficient for the corrosion rate evaluation. As a rule, several temperature regimes were established during one experiment. The post-test analysis included the measurement of the final corrosion depth, electromagnetic calculations, calculations of the melt thermo-hydrodynamics and specimen temperature distributions, as well as a package of physicochemical analyses of samples taken from the corium ingot and steel. The post-test analysis methodology is explained in detail in references [11, 12].

---

<sup>1</sup>  $C_n = 100(M_{Zr,\Sigma} - M_{Zr,met}) / M_{Zr,\Sigma}$ , %,

where  $M_{Zr,\Sigma}$  – total mass of Zr in corium;  $M_{Zr,met}$  – mass of unoxidized Zr

## Corium Session 2 – Paper 2.7

Table I shows the experimental matrix. Corium composition was varied in respect of oxygen content from suboxidized (with Zr-free) to fully-oxidized (U, Zr and Fe oxides with different valencies). Experiments with fully-oxidized corium were made in air and steam atmospheres above the melt; and experiments with suboxidized and close-to-stoichiometric coria – in a neutral atmosphere. Temperature at the corium-steel interaction interface was varied over a wide range but without reaching the liquidus temperature of steel.

**Table I: METCOR experimental matrix**

Test	Corium composition	Atmosphere	Melt temperature, °C	Specimen surface temperature, °C	Heat flux, MW/m <sup>2</sup>
MC1	(U, Zr)O <sub>2+x</sub> - FeO <sub>y</sub>	air	2700	950	0.9
MC2	(U, Zr)O <sub>2+x</sub> - FeO <sub>y</sub>	Air	2050...2350	720...1050	0.3...0.47
MC3	(U, Zr)O <sub>2</sub> - FeO	nitrogen	2100...2150	920...1220	0.28...0.48
MC5	C-100; (U, Zr)O <sub>2</sub>	argon	2600...2650	1075...1435	0.95...1.3
MC6	(U, Zr)O <sub>2-x</sub> (C-30)	argon	2400	1400*	1.23...1.31
MC7	(U, Zr)O <sub>2-x</sub> (C-30)	argon	2400	1150*	1.1
MC8	(U, Zr)O <sub>2-x</sub> (C-70)	argon	2450	1420*	1.35
MC9	C-30 and SS	argon	2450	1440*	1.1
MC10	(U, Zr)O <sub>2+x</sub> **	steam	2750...2800	1035...1235	0.95...1.1
MC11	(U, Zr)O <sub>2+x</sub> - FeO <sub>y</sub>	steam	1950...2100	950...1200	0.99...1.29
MC12	(U, Zr)O <sub>2+x</sub> - FeO <sub>y</sub>	air, steam	2000...2100	1000...1135	0.92...1.09
MCP-2	(U, Zr)O <sub>2+x</sub> **	Air	2700...2800	870...1370	0.74...1.19

\* – initial temperature on the interaction interface;

\*\* – initial composition.

The experiments with suboxidized corium [12, 13] having the composition, which can be conventionally described as UO<sub>2</sub>-ZrO<sub>2</sub>-Zr, have shown the following. During the initial incubation phase characterized by solid-phase diffusion an interaction zone (IZ) is established on the steel surface. The IZ is a thin layer accumulating corium components – it contains U, Zr, Fe, O and steel alloy admixtures; its composition is close to eutectic and its temperature exceeds the eutectic temperature. The formed liquid phase impregnates the corium crust and reduces its diffusion resistance. This, in turn, intensifies the mass transfer, i.e. corium components are transported into the IZ and steel components are transported into the corium; thus the steel corrosion rate increases. The incubation phase (of liquid phase formation) develops into the phase of fast corrosion. As a result of steel component dissolution (eutectic melting) the IZ boundary propagates in the direction of the cooler specimen bulk, the IZ boundary temperature falls, corrosion rate slows down, and the interaction reaches the saturation phase (Figure 1). Corrosion stops when the IZ boundary temperature and element concentrations reach the steel's final dissolution values in chemical equilibrium with corium under the thermal gradient conditions.

## Corium Session 2 – Paper 2.7

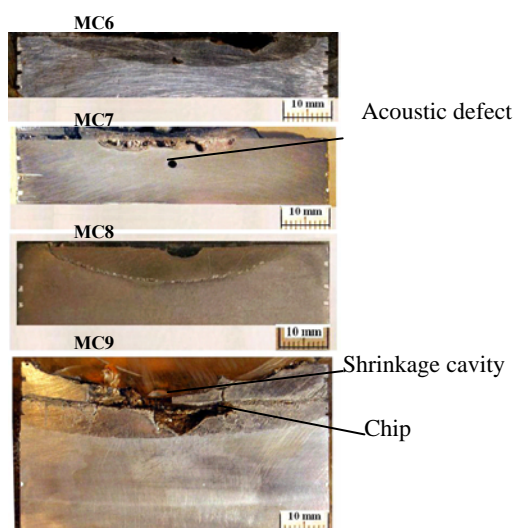


Figure 1: Axial sections of specimens after interaction with suboxidized corium

Therefore, the corrosion of steel by suboxidized molten corium can be presented as the components' partitioning between the oxidic ((U, Zr)O<sub>2-x</sub>) and metallic (U-Zr-Fe(Cr, Ni,...)-O) parts of the system, i.e. the interaction follows the mechanism determined by experiments within the MASCA project [9]. The difference was that in the MASCA tests chemical equilibrium was reached in the conditions close to thermodynamic equilibrium, and in METCOR experiments – under thermal gradient conditions. In contrast to the MASCA tests, the metallic part of the system (IZ in METCOR tests) was generally mushy (Figure 2). In the METCOR system the lack of isothermal conditions was indicated by much smaller U and Zr concentrations in the IZ in comparison to the MASCA metallic melt, other conditions being similar [15].

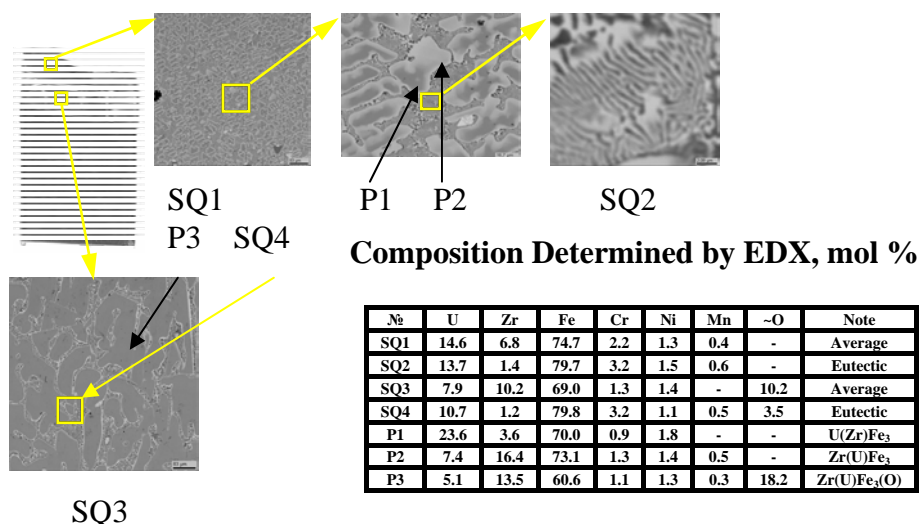


Figure 2: Microstructure and compositions of MC9 IZ

As mentioned before, the steel corrosion kinetics has three phases: incubation and acceleration (formation and accumulation of liquid phase, corium crust impregnation),

## Corium Session 2 – Paper 2.7

corrosion and then saturation. During the incubation phase the corrosion depth is negligible. The duration of this phase ( $t_{inc}$ ) mostly depends on the melt oxygen potential, which is characterized by Zr oxidation index  $C_n$ , and can be approximately described by correlation [13]

$$t_{inc}=8000+200(70-C_n), \text{ s}; \quad 70 \geq C_n \geq 30, \quad U/Zr \approx 1.2 \quad (1)$$

MC9 experiment had a shorter incubation phase. In this test stainless steel was added to the molten corium, which was followed by the components' (mainly Zr, U & Fe) repartitioning between the molten steel and oxidic melt, a heavier metallic melt then relocated to the pool bottom to interact with the steel specimen. It can be assumed that in this experiment the oxidic corium crust, which was originally formed on the steel surface, was impregnated not by the eutectic liquid produced on the steel surface, but by a Fe-rich U-Zr-Fe-(O) metallic melt.

Later, in a comparatively short period of time, the corrosion rate grows to reach its maximum value. A correlation for the main 2<sup>nd</sup> and 3<sup>rd</sup> phases of steady-state corrosion and saturation, during which its rate slows down (tending to zero), as the temperature on the progressing corrosion front decreases, was proposed in [13]. It has the following formulation:

$$W = 0.46 \cdot 10^{-7} \sqrt{T_{int} - T_B}; \quad 1440 \geq T_{int} \geq T_B, \quad 70 \geq C_n \geq 30, \quad U/Zr \approx 1.2 \quad (2)$$

Where  $W$  – corrosion rate, m/s;

$T_{int}$  – temperature on the corrosion front, °C;

$T_B$  – temperature of the final corrosion front position, °C.

The experimental minimum value of  $T_B$ , which is recommended for calculations, is 1090°C. Correlation (2) is applicable for conditions of the vessel steel interaction both with oxidic and metallic parts of the suboxidized corium pool.

As mentioned above, the mechanism of steel corruptions in its interaction with fully oxidized molten corium in an oxidizing above-melt atmosphere is principally different from the steel corrosion caused by the suboxidized corium in the inert atmosphere. Experiments with fully-oxidized corium in the oxidizing atmosphere have shown that steel corrosion is caused by its surface oxidation, and the corrosion rate has quite steady dynamics at a constant temperature on the interaction interface. The analysis of experimental data [11, 14, 16] resulted in the following model of the process.

The corium crust formed on the steel surface serves as the diffusion resistant layer to the transport of  $Fe^{2+}$  ions from steel into the melt. A high oxygen potential of the melt accounts for the counter-transport of  $O^{2-}$ , which does not limit the corrosion process. The thickness of solid crust depends on the thermal conditions and solidus temperature of corium. The crust liquefaction at temperatures below  $T_{sol}$  is possible for coria with high iron oxide content that can form low-temperature eutectics in the multi-component system including oxidic components of corium and steel (Figures 3, 4, 5 and 6). This phenomenon reduces the diffusion resistance of the crust and intensifies the corrosion.

## Corium Session 2 – Paper 2.7

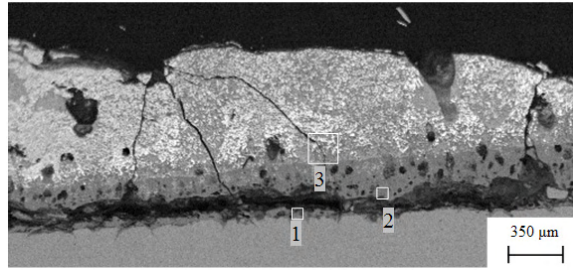


**Figure 3: SEM-Image of the Corium-Steel Interaction Zone with Regions Marked (1-3) where Higher Magnification Images Were Taken**

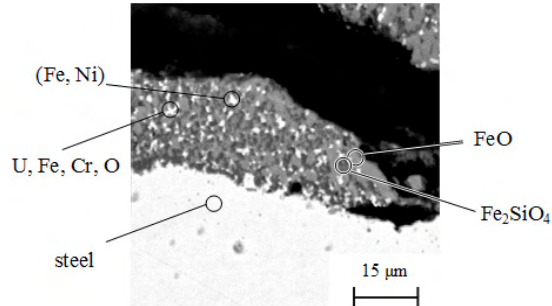


**Figure 4: SEM-Image of the Zone Adjacent to the Steel Surface (Region 1 in Figure 3)**

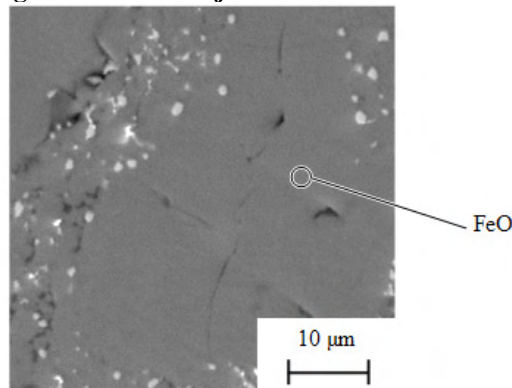


**Figure 5: SEM-Image of a Zone in the Corrosion Layer (Region 2 in Figure 3)**

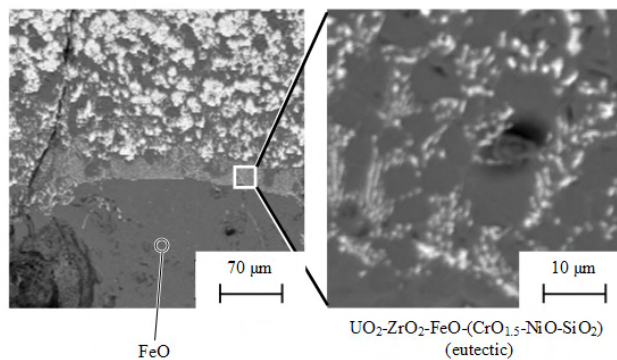


**Figure 6: SEM-Image of the Boundary Zone between Corrosion Layer and Corium Crust (Region 3 in Figure 3)**

It was found that the corrosion rate is sensitive to corium composition, but the difference between air or steam atmosphere has practically no influence.

## Corium Session 2 – Paper 2.7

The resulting corrosion rate correlations are as follows [16]:

For refractory (U, Zr)O<sub>2+x</sub> corium

$$\frac{W(2723 - T_S)}{q} = 4.98 \exp\left(-\frac{1.1 \cdot 10^5}{RT_S}\right). \quad (3)$$

And for fusible (U, Zr)O<sub>2+x</sub>-FeO<sub>y</sub> corium

$$\frac{W(1613 - T_S)}{q} = 0.1 \exp\left(-\frac{0.91 \cdot 10^5}{RT_S}\right) + 3.4 \cdot 10^{14} \exp\left(-\frac{4.99 \cdot 10^5}{RT_S}\right), \quad (4)$$

where W – corrosion rate, m/s;

q – heat flux, MW/m<sup>2</sup>;

R=8.314 J/(mol·K) – universal gas constant;

T<sub>S</sub> – temperature on the steel surface, K.

Ranges of application:

(U, Zr)O<sub>2+x</sub> corium: mass concentration FeO<sub>y</sub>=0...5%, atomic ratio U/Zr≈1.1, T<sub>S</sub>=870...1370 °C, q=0.74...1.19 MW/m<sup>2</sup>.

(U, Zr)O<sub>2+x</sub>-FeO<sub>y</sub> corium: mass concentration FeO<sub>y</sub>=20...30%, atomic ratio U/Zr=0.11...1.05, T<sub>S</sub>=720...1200 °C, q=0.3...1.3 MW/m<sup>2</sup>.

Experiments with (U, Zr)O<sub>2</sub> corium (C-100) in the argon atmosphere [12] have shown that the interaction causes practically no steel ablation almost up to its melting temperature. During the long-term interaction a thin layer of Fe<sub>1-x</sub>O is formed on its surface, which is followed by the eutectic steel melting (formation of a (U, Zr)O<sub>2</sub>-Fe<sub>1-x</sub>O-Fe melt); and the corrosion depth does not exceed several tenths of a millimeter.

Experiments with (U, Zr)O<sub>2</sub>-FeO corium, which also were carried out in the neutral atmosphere (nitrogen) [11], showed a more intensive interaction in comparison with C-100 corium. Its mechanism is similar to that of steel oxidation in air (without corium). The corrosion follows the parabolic law and produces a Fe<sub>1-x</sub>O layer on the steel surface. In the IVR conditions such mechanisms cannot lead to a considerable damage of the vessel wall, because the corrosion rate slows down rapidly.

## C APPLICABILITY TO IVR ANALYSIS

### C.1 Molten pool structure and heat transfer in corium molten pool

In this section the effect of vessel steel corrosion and its influence on the vessel integrity under the IVR conditions will be considered using a severe accident progression scenario using the VVER-1000 reactor as an example. Table II shows the masses of components, which are fully or partially involved into the molten pool formation in the reactor vessel.

**Table II: Masses of core components and in-vessel structures of VVER-1000**

Structures and components	Composition	Mass, t
Fuel	UO <sub>2</sub>	80.0
Fuel cladding	Zr – 1%Nb	24.0
Core structures (scram lines, separation grids)	SS	5.0
Control rods	B <sub>4</sub> C	0.43
Reactor bottom	Vessel Steel	33.3
Reactor side wall	Vessel Steel	79.4
Fuel assembly support	SS	10.0
Support grid	SS	4.0
Reactor shaft	SS	74.5
Partition	SS	35.8
Block of shielding tubes	SS	73.0

In accordance with estimates [17] a station blackout accident results in a molten pool formation of the following composition: UO<sub>2</sub>–76 t; ZrO<sub>2</sub>–11 t; Zr–14 t; SS–80 t (the initial mass of steel, after the vessel fails and a quasi-stationary state is reached, is about 100 t). Correspondingly, the Zr oxidation index is  $C_n \approx 35\%$ ; steel mass fraction  $\bar{m}_{st} = M_{ss} / M_{\Sigma} \approx 0.45$ ; atomic ratio U/Zr  $\approx 1.2$ .

From the results of ref. [9] it is known that at  $C_n = 30-45\%$  and small  $\bar{m}_{st}$  values the metallic melt is located in the molten pool bottom. But at  $\bar{m}_{st} \approx 0.3$  the metallic phase becomes lighter than oxidic part and forms a layer in the pool top; such a pool structure is therefore likely to form at  $\bar{m}_{st} \approx 0.45$ . As for the component partitioning between the oxidic and metallic liquids of the molten pool, the extrapolation of experimental data [9] for  $\bar{m}_{st} \approx 0.45$  has shown that U and Zr concentrations in the metallic melt are approximately 19 and 11 mass.%, respectively; the final oxidation index in the oxidic melt is  $C_n^f = 82\%$ . But a considerable temperature difference between the oxidic and metallic melts (800 – 1000°C cooler for the metallic melt) is expected to bring a more than twofold reduction of the above concentrations [13], with a corresponding  $C_n^f$  decrease to approx. 70%.

Assuming complete or partial melting of the components listed in Table II, the calculated volume of oxidic melt is  $V = 8.6 \text{ m}^3$ , and it practically coincides with the volume of semi-elliptical lower head ( $8.5 \text{ m}^3$ ). The volume of metallic melt is about  $16 \text{ m}^3$ , which corresponds to the height of this layer would have in the cylindrical part of the vessel ( $H = 1.2 \text{ m}$ ). Figure 7a shows a configuration of the oxidic-metallic pool. It should be noted that a probability of a three-layer pool structure [18] is still unclear, therefore the current paper considers only a two-layer structure of the suboxidized corium.

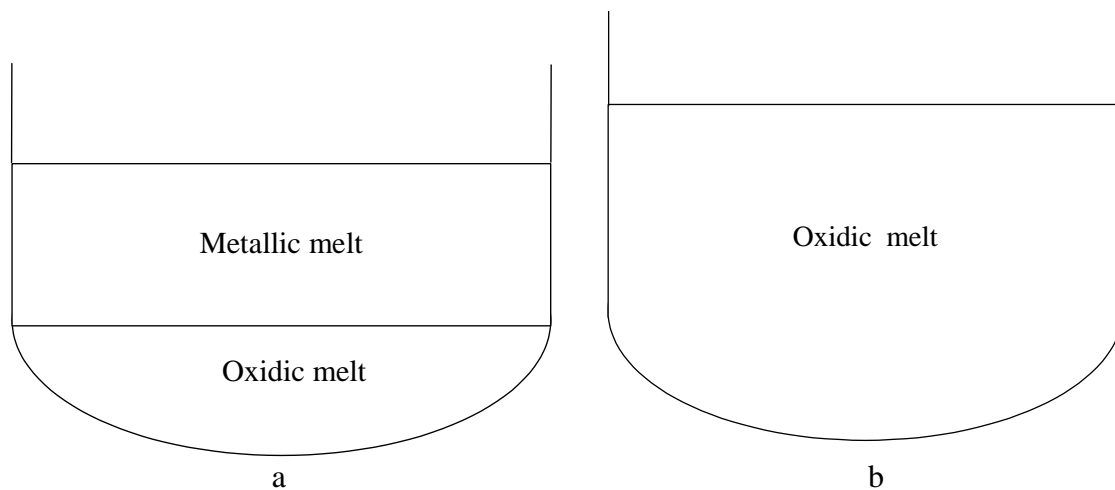


Figure 7: Molten pool configuration: a – stratified, b - homogeneous

A homogeneous pool of  $(U,Zr)O_{2+x}-FeO_y$  corium has been considered as an alternative. Such a pool is probable, if a steam/air atmosphere prevails in the reactor vessel. This can be the case, if water gets into the vessel in batches during the core degradation; it also is possible to have a gradual melting of the in-vessel structures without the formation of a stable steel layer on the pool surface, when, in accordance with [19], these structures are quickly oxidized in the oxidic melt. An additional oxidation of corium can also take place at the secondary melting of flooded debris in the reactor lower head.

A homogeneous oxidic melt containing the steel oxidation products has the mass of 210 t,  $5600 \text{ kg/m}^3$  density, and it occupies the volume of  $37.5 \text{ m}^3$ . The melt height in the cylindrical part of the reactor vessel is 2.12 m, and if we take the lower head into account – 3.1 m. Figure 7b gives the configuration of the homogeneous molten pool.

A model with lumped parameters based on the equation of energy balance was developed for calculating heat fluxes to the reactor vessel. In accordance with the free-convection schematics (Figure 8) the total volume of heat-generating fluid can be divided into two parts – the region with stable temperature stratification  $V_-$  and the region of instability  $V_+$ , caused by the convection of heat-generating fluid of Kulacki - Emara [20] at the adiabatic lower boundary. The convective transfer in this region is explained by the development of the Raleigh-Benard instability.

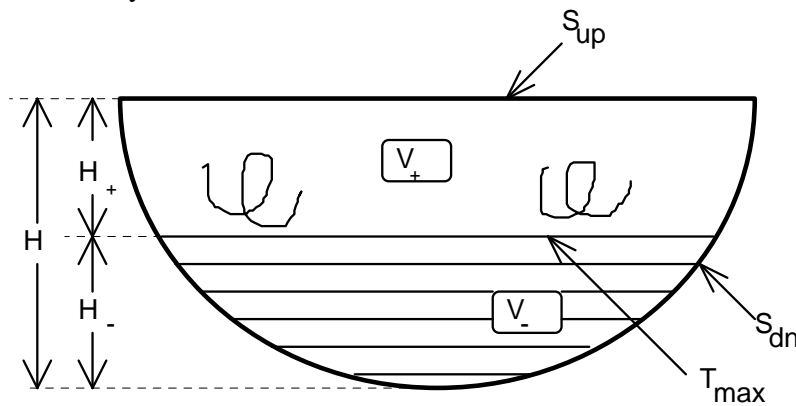


Figure 8: Free-convection schematics of the heat-generating fluid

The following correlation is valid for the oxidic layer:

$$\frac{\lambda}{H} \Delta T_{\max} \left( \text{Nu}_{\text{KE}} S_{\text{up}} \frac{H}{H_+} + \text{Nu}_{\text{dn}} S_{\text{dn}} \right) = Q_v V, \quad (5)$$

where  $Q_v$  – volumetric heat in the oxidic layer,  $\text{Nu}_{\text{KE}}$  and  $\text{Nu}_{\text{dn}}$  – average values of Nusselt numbers for the melt top and bottom surfaces,  $\lambda$  – heat conductivity and  $H$  and  $H_+$  are the total height and the height of the non-stratified zones respectively. The average values of Nusselt numbers to the cooled heat exchange surface in the oxide molten pool were calculated using the correlations for turbulent boundary layer [21]:

$$q = \frac{\lambda \Delta T_x}{x} \text{Nu}_x, \quad (6)$$

$$\text{Nu}_x = \frac{0.15(\text{Ra}_x)^{1/3}}{\left[ 1 + \left( \frac{0.492}{\text{Pr}} \right)^{9/16} \right]^{16/27}},$$

where  $x$  – coordinate along the boundary layer,  $\text{Pr}$  – Prandtl number,  $\text{Nu}_x$  and  $\text{Ra}_x$  – local numbers of Nusselt and Raleigh, respectively. The latter was calculated by  $\text{Ra}_x = \frac{g_x \beta \Delta T_x x^3}{\nu^2}$  taking into account the local temperature difference and projection of the gravitational acceleration  $g$  on the boundary layer direction,  $\beta$  – coefficient of volumetric expansion,  $\nu$  – kinematic viscosity.

The vertical distribution of temperature in the molten pool included in the expression for  $\text{Ra}_x$  number was modeled (parabolic profile) with a maximum value on the boundary between the regions with steady and non-steady temperature stratification. For the non-steady stratification region the constant temperature was approximated.

In the  $\text{Nu}_{\text{dn}}$  calculation the procedure of local heat-exchange coefficients approximation was used, which took into account the local temperature difference.

$$\text{Nu}_{\text{dn}} S_{\text{dn}} = \int_{S_{\text{dn}}} \text{Nu}_x \frac{\Delta T_x}{\Delta T_{\max}} dS. \quad (7)$$

The Kulacki-Emara convection is assumed in the top part of oxidic pool. The difference between this case and the classical Raleigh-Benard problem is in the presence of heat release in the region of non-steady temperature stratification. An approach described in [22] was used for combining the convective heat exchange of the heat-generating fluid with the Raleigh-Benard convection correlations. The same reference gives an overview of experimental data on the Raleigh-Benard convection, which, as a rule, are generalized as  $\text{Nu}_{\text{RB}} = C_{\text{RB}} \text{Ra}_{\text{RB}}^\alpha$ . We should note a rather large scattering both of  $\alpha$  values and the values of  $C_{\text{RB}}$ , which is barely influenced by the Prandtl number. At the adiabatic lower wall the convection of heat-generating fluid (Kulacki-Emara convection [20]) corresponds to the Raleigh-Benard convection for the half-thickness of the layer and half-temperature difference, as shown in Figure 9. As the heat flux in both cases should be the same, Nusselt numbers are correlated as follows

$$\text{Nu}_{\text{KE}}(H_+) \frac{\Delta T_{\text{KE}}}{H_+} = \text{Nu}_{\text{RB}}(H) \frac{\Delta T_{\text{RB}}}{H} \quad (8)$$

**Figure 9: Correlation of Kulacki-Emara (KE) and Raleigh-Benard (RB) models**

The relation of Raleigh numbers is set by correlation

$$\text{Ra}_{\text{RB}} = \frac{g\beta\Delta T_{\text{RB}}H^3}{\nu\chi} = \frac{g\beta\Delta T_{\text{KE}}H_+^3}{\nu\chi} \left(\frac{H}{H_+}\right)^3 \frac{\Delta T_{\text{RB}}}{\Delta T_{\text{KE}}} = 2 \left(\frac{H}{H_+}\right)^3 \text{Ra}_{\text{KE}}, \quad (9)$$

where  $\chi$  – temperature conductivity.

Using the correlation of  $\text{Nu}_{\text{RB}} = C_{\text{RB}}\text{Ra}_{\text{RB}}^\alpha$ , we get the following from (8) for the layer of heat-generating fluid:  $\text{Nu}_{\text{KE}} = C_{\text{KE}}\text{Ra}_{\text{KE}}^\alpha$ , where, in accordance with (9)

$$C_{\text{KE}} = 2^{1+\alpha} C_{\text{RB}} \left(\frac{H}{H_+}\right)^{3\alpha-1} = 2^{4\alpha} C_{\text{RB}}. \quad (10)$$

In order to determine the heat fluxes, the energy balance equation is written for the Raleigh number  $\text{Ra}$  calculated for the total height of the pool and a modified Raleigh number  $\text{Ra}_m$  as described in ref. [23]

$$\text{Ra} \frac{H}{V} \left( \text{Nu}_{\text{KE}} \frac{H}{H_+} S_{\text{up}} + \text{Nu}_{\text{dn}} S_{\text{dn}} \right) = \text{Ra}_m. \quad (11)$$

A model with lumped parameters was used for determining heat fluxes through the metallic melt, which was based on schematics shown in Figure 10.

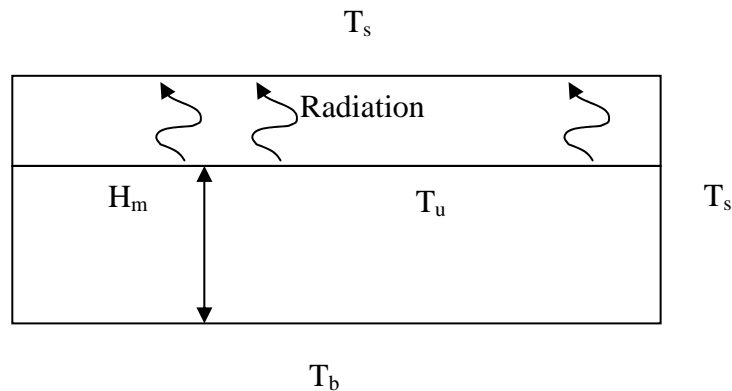


**Figure 10: Thermal model schematics of the surface metallic layer**

Heat flux from the top surface of the melt was determined by the Raleigh-Benard convection in accordance with equation [24] recommended for metallic layers in ref. [25] based on the BALI experiments:

$$Nu_{up} = 0.069Ra_1^{1/3} Pr^{0.074} = C_1 Ra_1^{1/3}. \quad (12)$$

Heat transfer with the lateral surface of metallic melt was calculated using equation (6):

$$Nu_{sd} = C_2 Ra_2^{1/3}. \quad (13)$$

The difference of Raleigh numbers is explained by the unequal temperature differences in the expression for Ra. For example, on the top surface  $S_{up}$  temperature  $T_u$  is determined by the conditions of radiation, and for the lateral, cooled surface  $S_{sd}$  the boundary temperature value is determined by the liquidus temperature of the metallic melt, and for the calculations it was assumed to be approximately equal to the temperature of steel vessel melting  $T_s$ .

For determining the top surface temperature it is assumed that the temperature of the surrounding structures is equal to the steel melting temperature  $T_s = 1730$  K with an effective emissivity  $\epsilon_{eff} = 0.43$ :

$$q_{up} = h(T_u - T_s) = \epsilon_{eff} \sigma (T_u^4 - T_s^4) = Bi \frac{\lambda}{H_m} (T_u - T_s). \quad (14)$$

The energy balance equation for metallic layer is as follows:

$$q_{down} S_d = Nu_{up} \frac{\lambda}{H_m} (T_b - T_u) S_{up} + Nu_{sd} \frac{\lambda}{H_m} (T_m - T_s) S_{sd}, \quad (15)$$

where  $T_m$  – average temperature of molten metal, which can be evaluated from a simple correlation:

$$\frac{T_m - T_u}{T_b - T_m} = \beta_0 \sim \left( \frac{q_{up}}{q_{down}} \right)^{\frac{3}{4}} = P^{\frac{3}{4}}, \quad (16)$$

where  $P$  is the fraction of the heat flux radiated from the melt surface.

## Corium Session 2 – Paper 2.7

In order to characterize the total heat transfer from the top surface the following parameter is introduced  $\alpha = \frac{Bi}{Bi + Nu_{up}}$ , where Bi – Bio number. The adiabatic top boundary has  $\alpha=0$  parameter, and the isothermal surface ( $Bi=\infty$ )  $\alpha=1$  parameter. Taking into account the metallic layer evaluation we get:

$$T_b - T_u = \alpha(T_b - T_s),$$

$$T_m - T_s = \left(1 - \frac{\alpha}{1 + \beta_0}\right)(T_b - T_s). \quad (17)$$

The cylindrical shape of the layer will transform the energy balance equation into:

$$q_{down} \frac{H_m}{\lambda} = Nu_{up}(T_b - T_u) + Nu_{sd}A(T_m - T_s), \quad (18)$$

where A-aspect ratio, which is equal to 2H/R for the cylindrical layer and H/R for the plane layer. The last-mentioned modification of A was applied for the model verification using the data from experiments with a flat (plane) layer. The substitution of temperature difference into the energy balance equation gives the following:

$$T_b - T_s = \frac{qH}{\lambda} \frac{1}{Nu_{up}\alpha + Nu_{sd}A\left(1 - \frac{\alpha}{\beta_0 + 1}\right)}. \quad (19)$$

After expressing the focusing factor as  $F = \frac{q_{sd}}{q_{down}} = \lambda Nu_{sd} \frac{T_m - T_s}{H_m q_{down}}$  we get the expression

$$F = \frac{Nu_{sd} \left(1 - \frac{\alpha}{\beta_0 + 1}\right)}{Nu_{up}\alpha + Nu_{sd}A\left(1 - \frac{\alpha}{\beta_0 + 1}\right)}. \quad (20)$$

The experimental data produced at the COPO facility, which simulated the VVER reactor vessel [26, 27], were used for the model verification.

The heat flux calculations for both molten pool configurations used the thermophysical melt properties given in Table III.

**Table III: Melt properties for the different pool configurations**

Parameter	Stratified pool		Single-liquid pool
	Oxidic melt	Metallic melt	
Solidus temperature, K	2500	1400	1560*
Liquidus temperature, K	2720	2000	2030
Density, kg/m <sup>3</sup>	7400	7245	5600
Heat conductivity, W/(m·K)	4.0	40**	3.5
Thermal expansion, 1/K	6.5·10 <sup>-5</sup>	3.2·10 <sup>-5</sup>	3.2·10 <sup>-5</sup>
Viscosity, Pa s	4.5·10 <sup>-3</sup>	3.3·10 <sup>-3</sup>	1.95·10 <sup>-2</sup>

## Corium Session 2 – Paper 2.7

Kinematic viscosity, m <sup>2</sup> /s	6.8·10 <sup>-7</sup>	4.5·10 <sup>-7</sup>	3.5·10 <sup>-6</sup>
Heat capacity, J/(kg·K)	600	660	720

\* - calculated using GEMINI2 code

\*\* - calculated by ideal solution model of U-Zr-Fe melt

As an example, Table IV gives some main parameters characterizing the heat load on the reactor vessel by the time of complete molten pool formation (approx. 8 hours after the accident start). At this point the decay heat power is 24 MW (0.8% of reactor capacity).

Figures 11 and 12 give the heat flux distribution in the oxidic molten pool (stratified and one-liquid cases).

The stratified pool has the maximum heat flux of 810 kW/m<sup>2</sup>, and the homogeneous pool 470 kW/m<sup>2</sup>. The calculated heat flux from the metallic layer of the stratified melt is about 870 kW/m<sup>2</sup>, and the reciprocal heat flux from the oxidic layer in this case is 1130 kW/m<sup>2</sup>, the calculated heat flux focusing coefficient is 0.77.

**Table IV: Heat fluxes for the considered molten pool configurations**

Parameter	Stratified pool		Single-liquid pool
	Oxidic melt	Metallic melt	
Volumetric heat, MW/m <sup>3</sup>	2.86	-*	0.64
Modified Re number	8.3·10 <sup>14</sup>	-	5.2·10 <sup>15</sup>
Nu <sub>up</sub>	1004	99.5	1374
Nu <sub>hr</sub> (for vertical surface)	721	172	1239
Nu <sub>dn</sub> (for horizontal surface)	501	-	1085
Upward heat flux, MW/m <sup>2</sup>	1.13	0.125	0.52
Maximum heat flux into vertical surface, MW/m <sup>2</sup>	0.81	0.87	0.47
Average** downward heat flux, MW/m <sup>2</sup>	0.564	1.13	0.41
Temperature difference***, K	281	152	324

\* - decay power in the metal melt (5-10 % of total power) is not considered for simplicity of the calculations

\*\* - averaged along the thermal boundary layer

\*\*\* - maximum difference across the boundary layer

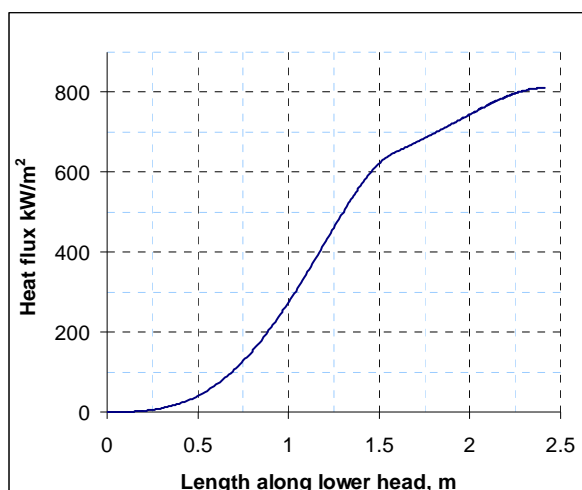


**Figure 11: Heat flux distribution along the vessel lower head for the oxidic layer of stratified pool**

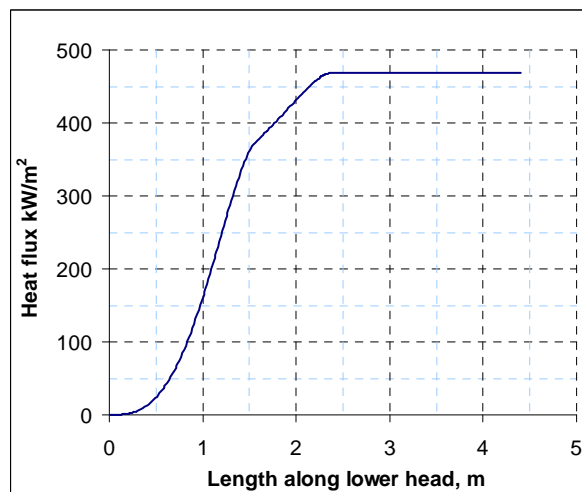


**Figure 12: Heat flux distribution along the vessel lower head for the single-liquid pool**

The subsequent vessel integrity analysis used the resulting heat flux distributions and its dynamics was coordinated with the decay heat evolution.

## C.2 Temperature, stress and strain field in the vessel wall

The integrity of the VVER-1000 RPV has been investigated using thermal and mechanical finite element calculations. Four scenarios are considered:

- A) the segregated melt pool without corrosion
- B) the segregated melt pool with corrosion (equation 2)
- C) the homogeneous melt pool without corrosion

## Corium Session 2 – Paper 2.7

D) the homogeneous melt pool with corrosion (equation 4)

In the first step the ablation of the vessel wall and the temperature fields in the wall are evaluated. It is assumed that the RPV is externally flooded. The thermal boundary conditions are the heat fluxes at the inner vessel surface as calculated in section C.1 and the outer surface temperature equals to 393 K.

The thermal calculation starts at 30000s after the beginning of the station blackout scenario. At this time the formation of the molten pool in the lower head is finished and the decay heat is about 24 MW. The corresponding heat flux distributions along the vessel wall are given in Figure 11 (scenarios A and B) and in Figure 12 (scenarios C and D). We start from a uniform vessel temperature of 393 K. In a first steady state solution step the temperature field is adjusted to the boundary conditions. The elements which exceed the melting temperature of the steel (1780 K) are removed (i.e. the material properties of those elements are switched: very high heat conductivity, very low density and specific heat capacity). After this the internal heat flux starts to decrease slowly in accordance with the decreasing decay heat. The heat fluxes from Figure 11 and Figure 12 are scaled down. Within 20 h they decrease by a factor of 0.69. In the scenarios A and C (no corrosion) the ablated steel mass remains constant. In the scenarios B and D the corrosion leads to a further ablation in spite of the decreasing wall temperature (Figure 15). A total time range of 20 h was analyzed.

Figure 13 and Figure 14 show the temperature field and the heat flux at the outer surface after 300 s and the final material configuration for the scenarios B and D. The upper part of the RPV including the upper head is also included in the model, but it is not shown.

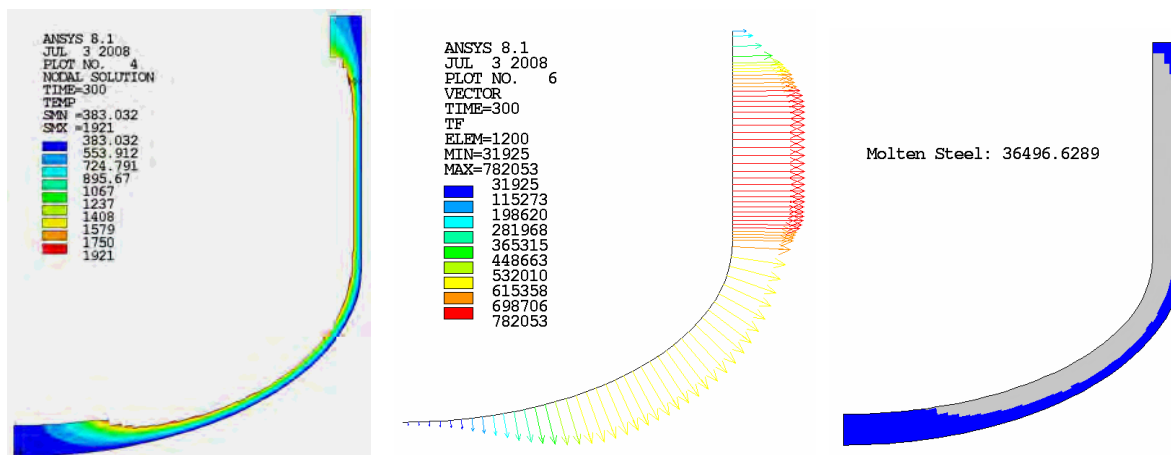


Figure 13: Scenario B, left: temperature field (K) at  $t = 300$  s, middle: heat flux at the external RPV surface ( $\text{W}/\text{m}^2$ ) at  $t = 300$  s, right: final material configuration (molten and ablated material is grey)

## Corium Session 2 – Paper 2.7

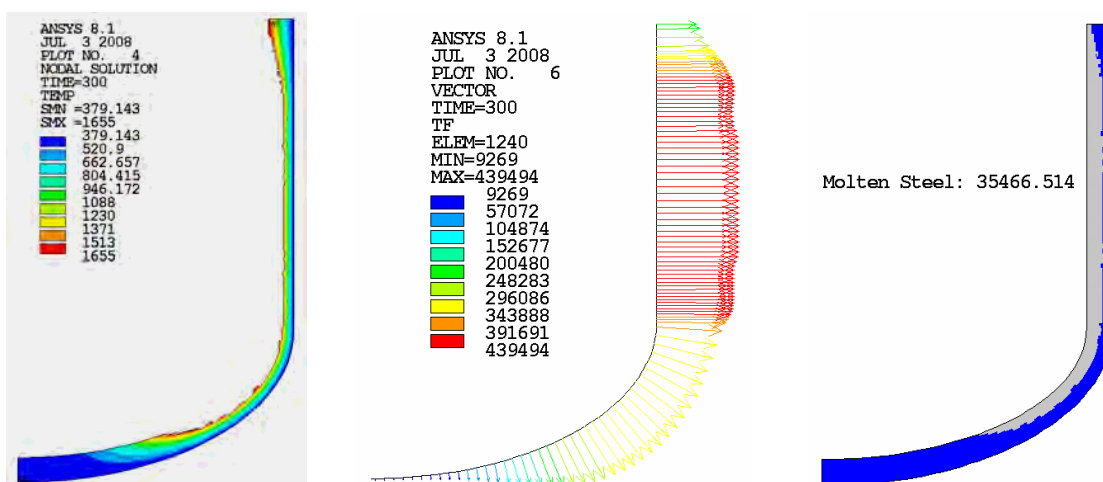


Figure 14: Scenario D, left: temperature field (K) at  $t = 300$  s, middle: heat flux at the external RPV surface ( $\text{W}/\text{m}^2$ ) at  $t = 300$  s, right: final material configuration (molten and ablated material is grey)

It can be seen that the outer heat flux into the water is somewhat smaller than the internal heat flux (Figures 11 and 12), which is mainly a consequence of the different inner and outer cylinder surface ( $q_{\text{int}} \cdot A_{\text{int}} \approx q_{\text{ext}} \cdot A_{\text{ext}}$ ).

Figure 15 shows the progression of the ablation of the RPV wall with time. As mentioned above, in the scenarios with corrosion we observe wall erosion while the temperature level in the vessel is already decreasing. Comparing the scenarios B and D it can be seen, that in the case of the fully oxidized corium (D) the effect of corrosion is more pronounced and occurs earlier in time than in the case of the suboxidized pool (B), although the latter has the larger final ablation depth. In both cases the corrosion becomes negligible when the temperature of the remaining vessel wall sinks below 1363 K (Fig. 14 – left and right).

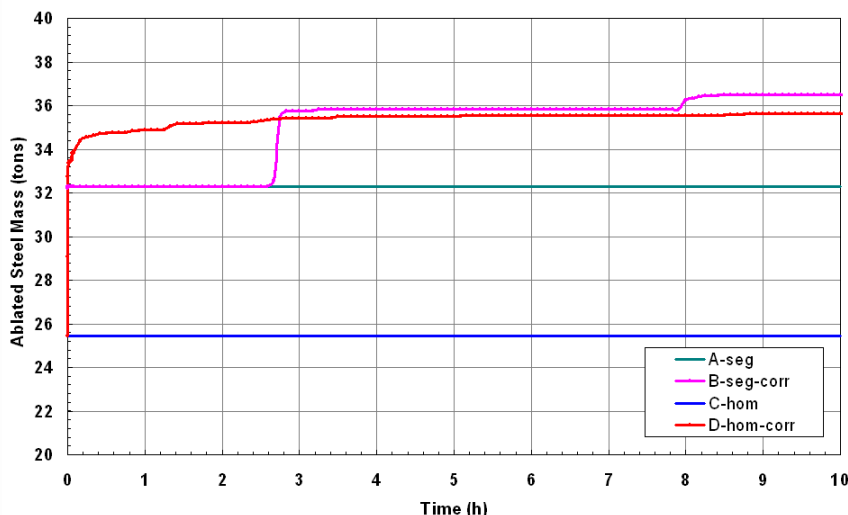
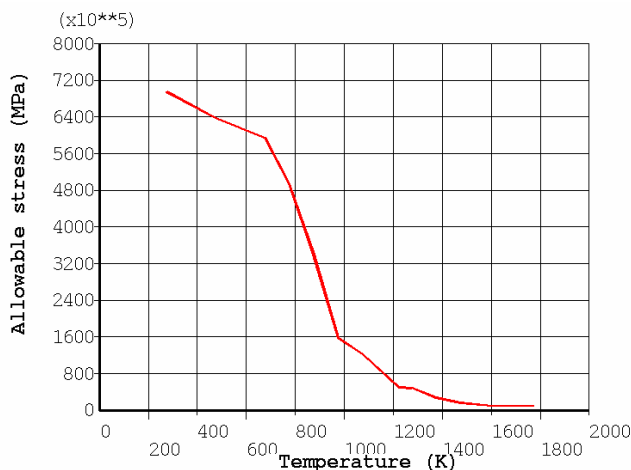


Figure 15: Ablation of RPV steel vs. time,  $t = 0$  s denotes the end of the pool formation period

In the following finite element (FE) mechanical analysis, the internal pressure at which the RPV would fail for different scenarios is evaluated. For this purpose we performed elastic-plastic calculations with increasing pressure until vessel failure. The material data base

## Corium Session 2 – Paper 2.7

was elaborated in earlier works based on high temperature creep and tensile tests [28, 29]. The temperature dependent allowable stress is shown in Figure 16. It is assumed that the vessel fails when a certain maximum (or allowable) stress is exceeded in the outer part of the vessel wall.



**Figure 16: Allowable stress versus temperature for the RPV steel. It corresponds to the true ultimate strength used in the plasticity model**

The results are shown in Figure 17 (scenarios A and B) and Figure 18 (scenarios C and D). It can be seen that the stress distribution in the outer wall region hardly depends on the fact whether or not corrosion takes place. In spite of the different remaining wall thicknesses in scenario A and B the pressures at vessel failure are almost identical. The same is true for the scenarios C and D.

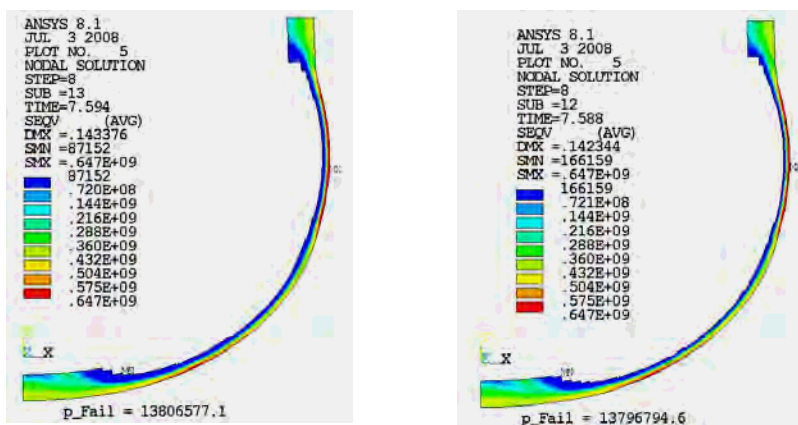


**Figure 17: Equivalent stress [Pa] in the RPV wall at failure pressure left scenario A, right scenario B**

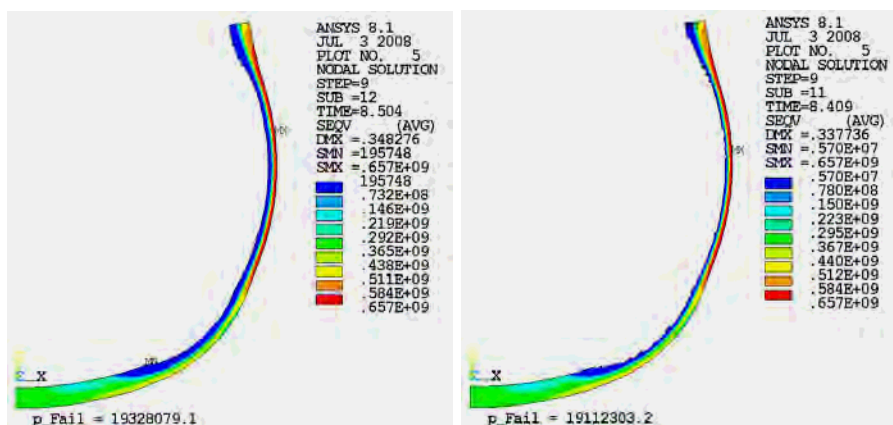


Figure 18: Equivalent stress [Pa] in the RPV wall at failure pressure left scenario C, right scenario D

Table V gives an overview of the main results of the thermal and mechanical FE calculations.

Table V: Main results of the thermo-mechanical RPV simulations for scenarios A-D

Scenario	A	B	C	D
Pool configuration	segregated (Figure 7a)	segregated (Figure 7a)	homogeneous (Figure 7b)	homogeneous (Figure 7b)
Corrosion	no	equation 2	no	equation 4
Ablated steel mass	32.3 t	36.5 t	25.5 t	35.5 t
Min. wall thickness	60 mm	50 mm	100 mm	70 mm
Pressure of failure	13.81 MPa	13.80 MPa	19.33 MPa	19.11 MPa

It can be seen that corrosion leads to a significantly higher vessel wall ablation. The remaining wall thickness is therefore smaller when the corrosion is considered. This effect is more significant in the case of the fully oxidized (homogeneous) corium pool. Nevertheless the influence of corrosion on the mechanical strength of the RPV is negligible. The reason is the strong temperature gradient over the vessel wall thickness. The internal part is hot, i.e. close to the liquidus temperature of the steel for cases A and C or close to the corrosion limit temperature for cases B and D. So there is nearly no material left to carry any relevant load at the inside wall. The load, consisting of dead weight and internal pressure, is carried almost completely by the external wall layer, because this layer is cooled by the external flooding and therefore retains a much higher strength.

## D Concluding Remark

An analytical technique has been developed and has clarified the role of corrosion and temperature on the failure strength of a reactor vessel; it demonstrates how the vessel's resistance is critically dependent on the cool outer skin of the vessel. This analysis can be applied to other IVR scenarios/vessels as part of the safety evaluation process.

## REFERENCES

- [1] O. Kymalainen, H. Tuomisto, T.G. Theofanous, In-vessel retention of corium at the Loviisa plant, *J. Nuc. Eng. and Design*, 169, pp. 109-130 (1997).
- [2] T. G. Theofanous, C. Lin, S. Addition et al., In-Vessel Coolability and Retention of a Core Melt, *J. Nucl. Eng. and Design*, 169, pp. 1-48 (1997).
- [3] M. F. Rogov, S. A. Loginov, V. S. Granovsky et al., Analyzing the Possibility of Retaining the Corium in the Vessel of a VVER-640 Reactor in a Severe Accident with a Damage Core, *J. Thermal Engineering*, v.43, #11, pp. 888-892 (1996).
- [4] W. Brettschuh, SWR 1000: An advanced, Medium-Sized Boiling Water Reactor, Ready for Deployment, *Proc. of ICAPP 06, Reno, USA* (2006).
- [5] S. J. Oh, K. C. Parc and H. G. Kim, Advanced Design Features of APR 1400 and Realization in Shin Kori Construction Project, *Proceeding of ICAPP'06, Reno, USA* (2006).
- [6] T. N. Dinh, J. P. Tu and T. G. Theofanous, Two-Phase Natural Circulation Flow in AP-1000 In-Vessel Retention-Related ULPU-V Facility Experiments, *Proceeding of ICAPP'04, Pittsburgh, PA USA* (2004).
- [7] T. G. Theofanous et al., In-Vessel Coolability and Retention of a Core Melt, *DOE/ID-10460* (1996).
- [8] K. Froment, J. M. Seiler, C. Gueniau et al., Physico-Chemistry and Corium Properties for In-Vessel Retention, In-Vessel Core Debris Retention and Coolability. Workshop Proceedings 3-6 March 1998, Garching near Munich, Germany (1998).
- [9] V. G. Asmolov, S. V. Bechta, V. F. Strizhov et al., Partitioning of U, Zr and Fe between Molten Oxidic and Metallic Corium, *Proceedings of MASCA Seminar 2004, Aix-en-Provence, France* (2004).
- [10] Yu. B. Petrov, *Induction Melting of Oxides*, L.: Energoatomizdat, (1983), (In Russian).
- [11] S. V. Bechta, V. B. Khabensky, S. A. Vitol et al., Corrosion of vessel steel during its interaction with molten corium. Part 1: Experimental, *J. Nucl. Eng. Design*, 236, pp. 1810-1829 (2006).
- [12] S. V. Bechta, V. B. Khabensky, V. S. Granovsky et al., New Experimental Results on the Interaction of Molten Corium with Reactor Vessel Steel, *Proceeding of ICAPP'04, Pittsburgh, PA USA* (2004).
- [13] S. V. Bechta, V. B. Khabensky, V. S. Granovsky et al., Experimental Study of Interaction Between Suboxidized Corium and Reactor Vessel Steel, *Proceeding ICAPP'06, Reno, USA* (2006).
- [14] S. V. Bechta et al., Interactions of  $UO_{2+x}$ - $ZrO_2$ - $FeO_y$  corium melt with vessel steel of VVER reactor, *Proceedings of ICAPP'08, Anaheim, USA* (2008).
- [15] S. V. Bechta et al., Corium Phase Equilibria from MASCA, METCOR and CORPHAD Results, *J. Nucl. Eng. Design* (in press).
- [16] S. V. Bechta, V. B. Khabensky, V. S. Granovsky et al., VVER Vessel Steel Corrosion at Interaction with Molten Corium in Oxidizing Atmosphere (to be published).
- [17] V.V. Bezlepkin, E.Yu. Kuzmin, A.E. Kiselev, V.F. Strizhov et al. Investigation of the in-vessel lower head melt retention at a late phase of the severe accident development using the RATEG/VSECHA/GEFEST code. *Newsletter of atomic science and technology. Series: Physics of nuclear reactors, Issue. 4, CC. 20 – 28* (2003), (in Russian).

## Corium Session 2 – Paper 2.7

- [18] J. M. Seiler, B. Tourniaire, F. Defoort, K. Froment, Analysis of In-Vessel Retention with Special Interest in Physico-Chemistry Effect, Proceeding ICAPP'05, Seoul, Korea (2005).
- [19] S. V. Bechta, V. B. Khabensky, S. A. Vitol et al., Experimental studies of oxidic molten corium – vessel steel interaction, J. Nucl. Eng. Design, 210, pp. 193-224 (2001).
- [20] F. A. Kulacki, A. A. Emara, Steady and transient thermal convection in a fluid layer with uniform volumetric energy sources. J.Fluid Mech, 83, pt.2, pp. 275–295 (1977).
- [21] S. W. Churchill and H. H. S. Chu, Correlation equations for laminar and turbulent convection from a vertical plate, Int. J. Heat Mass Transfer, 18, 1323 (1975).
- [22] L. Bernaz, J. M. Bonnet, J. M. Seiler, Investigation of natural heat transfer to the cooled top boundary of a heated pool. 9-th Int. Topical Meeting on Nuclear reactor thermal hydraulic (NURETH-9), 1999.
- [23] L.A. Bolshov, P.S. Kondratenko, V.F. Strizhov, Free convection of heat-releasing liquid, Achievements of physics, 171, #10, 1051-1070 (2001), (in Russian).
- [24] S. Globe and D. Dopkin, Natural circulation heat transfer in liquids confined by two horizontal plates and heated from below, J. of Heat transfer, 81, 24-28 (1959).
- [25] J. M. Bonnet, J. M. Seiler, Thermal hydraulic phenomena in corium pools. The BALI Experiment. 7-th International Conference on Nuclear Engineering Tokyo, Japan, April 19-23, ICONE-7057 (1999).
- [26] O. Kymalainen, H. Tuomisto, O. Hongisto, T. Theofanous. Heat flux distribution from a volumetrically heated pool with high Raleigh number, Proceeding NURETH 6, Grenoble, France, pp. 47 – 53 (1993).
- [27] M. Helle, O. Kymalainen, E. Pessa, COPO II – Lo Experiments, Report IVO Power Engineering LTD, October (1997).
- [28] Willschuetz H.G. et al, Simulation of creep tests with French or German RPV-steel and investigation of a RPV-support against failure. Annals of Nuclear Energy 30, 1033-1063 (2003).
- [29] Sainte Catherine C., Tensile and creep tests material characterization of RPV steel at high temperatures. Rapport SEMT/LISN/RT/98-009/A, CEA (1998).